OPEN ACCESS
IOP Publishing
Smart Materials and Structures
Smart Mater. Struct. **26** (2017) 115014 (17pp)
https://doi.org/10.1088/1361-665X/aa8753

A new class of variable capacitance generators based on the dielectric fluid transducer

Mattia Duranti[1], **Michele Righi**[2], **Rocco Vertechy**[3] and **Marco Fontana**[4]

[1] Industrial Engineering Department, University of Trento, Trento, IT, Italy
[2] TeCIP Institute, Scuola Superiore Sant'Anna, Pisa, IT, Italy,
[3] Industrial Engineering Department, University of Bologna, Bologna, IT, Italy
[4] Industrial Engineering Department, University of Trento, Trento, IT, Italy

E-mail: marco.fontana-2@unitn.it

Received 30 April 2017, revised 6 August 2017
Accepted for publication 21 August 2017
Published 9 October 2017

Abstract

This paper introduces the novel concept of dielectric fluid transducer (DFT), which is an electrostatic variable capacitance transducer made by compliant electrodes, solid dielectrics and a dielectric fluid with variable volume and/or shape. The DFT can be employed in actuator mode and generator mode. In this work, DFTs are studied as electromechanical generators able to convert oscillating mechanical energy into direct current electricity. Beside illustrating the working principle of dielectric fluid generators (DFGs), we introduce different architectural implementations and provide considerations on limitations and best practices for their design. Additionally, the proposed concept is demonstrated in a preliminary experimental test campaign conducted on a first DFG prototype. During experimental tests a maximum energy per cycle of 4.6 mJ and maximum power of 0.575 mW has been converted, with a conversion efficiency up to 30%. These figures correspond to converted energy densities of 63.8 mJ g^{-1} with respect to the displaced dielectric fluid and 179.0 mJ g^{-1} with respect to the mass of the solid dielectric. This promising performance can be largely improved through the optimization of device topology and dimensions, as well as by the adoption of more performing conductive and dielectric materials.

Keywords: dielectric fluid, variable capacitance, electrostatic generator, electrostatic transducer, dielectric elastomer

(Some figures may appear in colour only in the online journal)

1. Introduction

The static coupling between electrical and mechanical energy has been extensively studied for the implementation of sensors, actuators and generators, often referred to as electrostatic transducers. These devices are based on a main core component that is a mechanically variable capacitor (MVC), i.e. a capacitor whose capacitance can change significantly as a result of the application of a mechanical input. Such a change in capacitance makes it possible to sense displacements/forces/pressures [1], to produce actuation forces [2, 3] or to convert mechanical energy into DC electricity [4–6].

Differently than electromagnetic systems, operation of electrostatic transducers as actuators and generators is cyclical in nature and often requires that a priming energy is applied to the MVC prior to the beginning of the cycle. In most cases, the amount of energy that will be converted from mechanical to electrical, and/or vice versa, will be a multiple of this priming energy. Although the priming energy can often be recovered after the operation cycle, it should be considered as a cost and, thus, be reduced as much as possible as compared

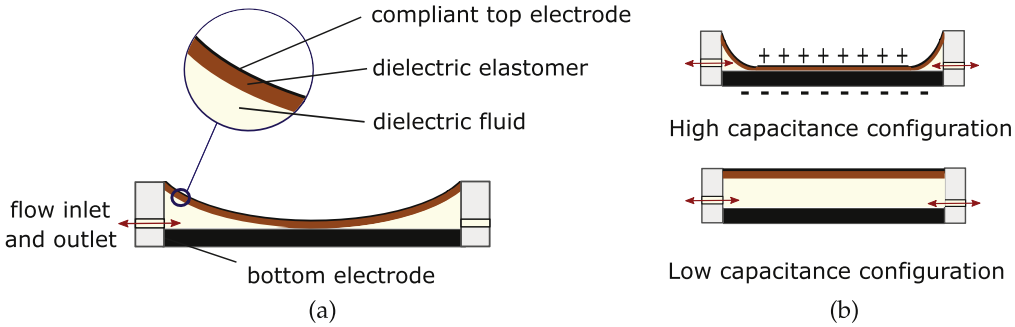

Figure 1. Scheme of the analyzed dielectric fluid transducer (defined in the following as a cCFr architecture). Figure 1(a) shows a simplified design of the proposed DFT concept. Figure 1(b) shows the two extreme configurations in the capacitance range.

to the converted energy. For example, for given values of converted energy and efficiency of the priming electronics, an increase in the priming energy determines a proportional increase in the energy losses. Thus, in general, to enhance the global efficiency it is required to maximize the ratio between converted and priming energy, or to improve the performance of the electronics using more complex solutions for the driving circuitry.

The implementation of MVC can be achieved with alternative techniques, according to the requirements of the different applications. In the first examples of MVCs the variation of capacitance is achieved through the relative displacement of the rigid armatures of the capacitor or through the displacement of dielectric materials between the armatures. In 2000, highly deformable capacitors, made of elastic dielectrics and compliant electrodes, have been introduced under the name of dielectric elastomer transducers (DET) [7]. This kind of device has been intensively investigated in the last decade due to promising attributes, such as high energy density, good conversion efficiency and low cost [8–12]. Very recently, transducers involving electrets combined with elastic dielectrics and compliant electrodes have been investigated with the aim to harvest electricity from ambient low density energy sources [13].

In this context, this paper presents and investigates a MVC transducer that relies on the variation in volume of a dielectric fluid. Although electromechanical coupling between fluids and electrical fields is known since the end of nineteenth century [14–17], previous studies only have considered devices where the change in capacitance is implemented through the movement of a fluid between fixed stiff electrodes, such as the dielectrophoretic pumps [18, 19].

In this contribution instead, the capacitance modulation is obtained by means of a pressurized dielectric fluid that stretches apart and separate the compliant electrodes of a variable volume capacitor. Hereafter, this concept is referred to as dielectric fluid transducer (DFT). Since the variable capacitance enables the bidirectional conversion of mechanical energy into electricity, the considered DFT can be used as actuator, sensor or generator.

The deformable parts of a DFT can be manufactured using low cost materials and processes, that are typically employed for DETs [20, 21]. As for the adopted fluid, there are several alternatives among chemical compounds that are widely used in industrial applications, such as dielectric insulators for transformers [22, 23].

As compared to MVC transducers based on fixed armature and moving dielectric, DFTs provide the following advantages: (1) the ratio of converted and priming energy depends on volume variation, which can be made very large, and is not limited by the permittivity ratio of dielectric and air; (2) the amount of priming energy (and, thus, of the converted energy) is not limited by the dielectric strength of air, but is function of the dielectric strength of the adopted dielectric that is usually larger. As compared to MVC transducers based on rigid and moving armatures, DFTs enable: (1) straightforward implementation of the moving armature without the need of complicated and bulky mechanisms and load-bearing systems; (2) intrinsic realization of a tight sealing system that makes it possible to employ fluid dielectric in place of air, thereby increasing the converted energy of the device.

As compared to DETs, DFTs: (1) can potentially feature a larger ratio between converted and stored elastic energy, which makes it possible to decrease the mechanical energy input required to operate the device, as explained in section 2.1; (2) are potentially less affected by the dielectric strength of the employed material since the electrical breakdown in liquids is often reversible while in solids it is not.

DFTs can be potentially employed in a number of different applications, including many of those suited for DETs. More specifically, in actuation mode they could provide the fluid displacement to drive different types of hydraulic systems, such as linear or rotary actuators, valves and more general deformable structures, which are employed in soft robotics and mechatronics. In generation mode, DFTs can be easily implemented for energy harvesting wherever an oscillating pressure is available, such as in the case of low-density wind generators, wave energy generators and human energy harvesters.

The present work is specifically focused on the study of a DFT in generation mode, that takes the name of dielectric fluid generator (DFG). In particular, we developed and tested a proof of concept prototype of DFG. This device is a parallel plate capacitor, in which a dielectric fluid is pumped to separate a non-conductive circular membrane, that is painted on the external side with conductive carbon grease (compliant electrode), from a flat metallic plate (bottom electrode)—see

figure 1. This design leads to a considerable variation in capacitance, due to a large relative modification of the contact area between the membrane and the metallic electrode.

Low costs of the basic component and the level of performance obtained in the experiments, conducted with such a preliminary prototype, suggest that this new class of generators can grow into a promising type of energy converters with large potential for future applications.

The contents of this paper are organized as follows. Section 2 describes the DFT working principle, focusing on the operation in generation mode, and provides a discussion on performance and materials. Section 3 presents a proof of concept prototype and the test bench employed for its operation. Section 4 reports the results of the first campaign of experimental tests, evaluating the performance of the system. Section 5 draws conclusions and future perspectives.

2. Concept description

2.1. Working principle and architectures

A DFT is a capacitor with a highly variable shape that uses a non-conductive fluid as a dielectric that penetrates in between a pair of variable geometry electrodes. Figure 1 shows the cross-section of a simple axisymmetric DFT that features a cylindrical chamber, filled with a dielectric fluid, which is enclosed at the top by a circular dielectric elastomer membrane with a deposited deformable electrode on its upper face and at the bottom by a second flat and rigid circular electrode. The upper deformable membrane, fixed along its perimeter to the annulus shaped support that delimits the lateral surface of the fluid chamber, can be deflected and squeezed on the bottom rigid electrode, thereby increasing the transducer capacitance.

Pumping the fluid in/out of the chamber enables the deformable electrode to shift smoothly from the rigid electrode, thereby making the DFT to pass from a high capacitance configuration (maximum contact area between upper deformable membrane and bottom rigid electrode) to another, which has order of magnitude lower capacitance (null contact area as shown in lower schematic of figure 1(b)). In the first configuration (upper schematic in figure 1(b)), the fluid film thickness is practically null, and the electrodes surfaces are only separated by the dielectric elastomer membrane having an approximately constant thickness, while in the second position (lower schematic in figure 1(b)), the fluid layer thickness is maximum.

As shown in figure 1(a), in any other intermediate operative configuration, the thickness of the fluid layer is not uniform in the device. In particular, in going from the low to the high capacitance configuration, the elastic membrane comes in contact with the flat rigid electrode at one single point first (with the fluid film thickness being finite and different at all other locations) and, then, the contact extends to the full electrode surface (thereby making the fluid film thickness zero everywhere).

As compared to DETs, a first major advantage of DFTs is a reduced deformation required by electrodes and dielectrics to obtain a large capacitance variation. This means that, for a same energy output, DFTs require a lower input of mechanical work and exhibit a lower mechanical impedance. Second, being based on dielectric fluids, DFT can potentially enjoy enhanced lifetime provided by self-healing capacity against dielectric breakdown. This is due to the fact that (1) breakdown fields of dielectric fluids are generally lower than that ones of dielectric solids, thus the conductive path will be established more likely in the dielectric fluid, without the involvement of the dielectric solid and (2) electrical breakdown causes irreversible failure only in dielectric solids, whereas in fluids the non-conductivity of the broken layer can often be recovered in some time after the deactivation of the transducer [24].

However, a fair comparison with DETs should also consider some potential drawbacks. The most obvious are the limitations that could be determined by the fluid viscosity. In general, although the losses due to viscoelasticity are expected to be lower than DETs, the losses due to the fluid viscosity can be relevant. In particular, the fluid motion is associated with a reduction in the efficiency and can determine bandwidth limitations for both actuation and generation applications. This drawback could be mitigated by the employment of optimized shapes for fluid flow and by the usage of low-viscosity dielectric fluids.

In addition to the embodiment shown in figure 1, the DFT concept can also be implemented by choosing several other alternative architectures with some common elements: two electrodes with at least one of them being compliant, a layer of dielectric fluid, and a layer of dielectric solid which can be either rigid or compliant. The resulting different architectures can be easily named by using an ordered string of letters which provides the sequence of different layers. Specifically, we use the letters R or C and F, respectively standing for rigid, compliant and fluid dielectrics, and the corresponding small letter for identifying conductive layers. Thus, the example provided in figure 1 can be named as cCFr DFT. Other alternative architectures with their identification strings are provided in figure 2.

It is worth to notice that some elements must be common to each architecture:

- *Two or more, never odd, electrodes with at least one of them being deformable:* the device can be made up of a single deformable electrode squeezed on a rigid flat electrode (figures 2(a), (c)), or by two deformable electrodes that squeeze one on the other (figures 2(b), (d)).
- *One or more layers of dielectric fluid;*
- *At least one non-conductive solid layer between electrodes:* the deformable electrodes can be alternatively made by a conductive elastomeric membrane directly in contact with the dielectric fluid (figures 2(c), (d)), or deposited on the upper surface of a dielectric elastomer (figures 2(a), (b)). In the first case, the dielectric fluid must be bottomed with a rigid non-conductive layer that prevents the two electrodes from coming into direct contact. This solid

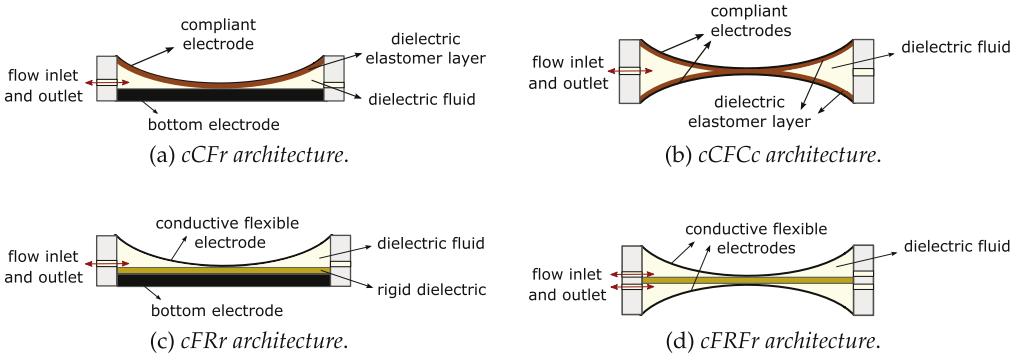

(a) *cCFr architecture.* (b) *cCFCc architecture.*

(c) *cFRr architecture.* (d) *cFRFr architecture.*

Figure 2. Four examples of dielectric fluid transducer (DFT) architectures. In cCFr and cCFCc (figures 2(a) and (b)) the flexible electrodes are realized over a dielectric elastomer support layer with the compliant electrode laying on the external side of the transducer. In cFRr and cFRFc (figures 2(c) and (d)) the electrodes are fully made with a conductive polymer and remain separated by a rigid dielectric layer.

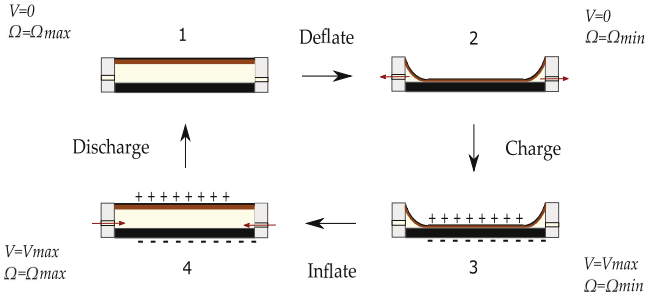

Figure 3. Scheme of the generating cycle of a DFG. V is the voltage between the electrodes and Ω is the volume of the fluid in the variable volume chamber. The considered cycle is composed by two isopotential phases, i.e. deflection and inflation (or generation), and two isochoric phases, i.e. priming and discharging.

dielectric layer, with strong breakdown resistance properties alike mica or glass, may also be used to adjust the DFT capacitance.

Stacks of DFTs of these kinds can be implemented, possibly obtaining systems with an odd number of electrodes.

In the remainder of this work we present the modeling, implementation and experimentation of a DFG having the cCFr architecture shown in figure 1. In particular, from bottom to top, the system is composed by a rigid metallic electrode, a dielectric fluid and a dielectric elastomer membrane with a compliant electrode layer on its upper side.

2.2. Generator mode: theory of operation

In this section, we explore the operation and the limits of a DFG. First, a simple operation mode is presented. Second, the limits of operation provided by the physical properties of materials are illustrated.

2.2.1. Working cycle and physical principle. The simplest generating cycle can be obtained by two constant voltage processes, i.e. isopotential, and two constant volume processes, i.e. isochorics. This cycle, represented in figure 3 and drawn in figure 4 with the red lines, features the following phases:

- (1–2) *Capacitance increase:* during this phase the elastic membrane bends at constant null voltage, driven by a negative fluid pressure, and squeezes on the rigid flat electrode increasing the DFG capacitance; some mechanical work is transferred from the fluid to the membrane and stored in the form of elastic energy;
- (2–3) *Priming:* during this phase opposite charges are transferred to the two electrodes until a target voltage is reached, whereas the amount of fluid in the chamber is kept constant; transfer of charges is performed by an external power supply; part of the electrical work done by this supply is stored by the DFG in the form of electrostatic energy;
- (3–4) *Generation:* during this phase the membrane is pushed back to its undeformed state by an increasing fluid pressure, whereas the voltage is kept constant; the distance between electrodes increases, thus the capacitance of the DFG decreases, which makes some charges be ejected from the electrodes; the elastic energy is recovered and part of the mechanical work done by the fluid and of the priming energy are transferred out of the system;
- (4–1) *Discharge:* during this phase, charges are removed from the electrodes until a null voltage is reached, whereas the volume of fluid in the chamber is kept constant; the remaining part of the electrostatic priming energy is removed from the system.

Similar to the operation of DETs [7], this is only one of the several energy harvesting cycles that can be implemented on a DFG. In particular, the generation phase might also be performed by maintaining transducer electrodes at either constant voltage, constant charge or constant electric field with a general time profile of the inlet fluid flow rate. Each one of the latter options gives a different amount of harvested energy. The generation cycle at constant voltage is considered here for its simplicity and because it can be extended to match well the DFT working limits (see section 2.2.2).

Henceforth, we define with ϵ, ε and E the absolute permittivity, relative permittivity and electric field of the

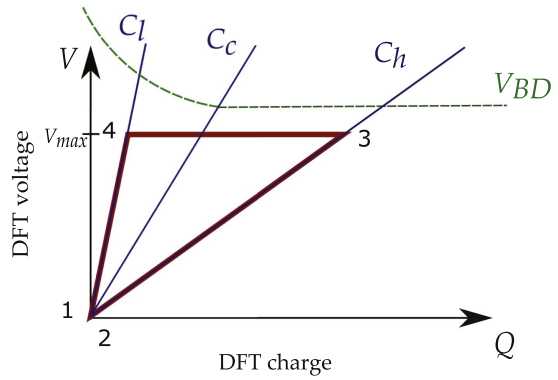

(a) Voltage V between the electrodes vs. stored charge Q

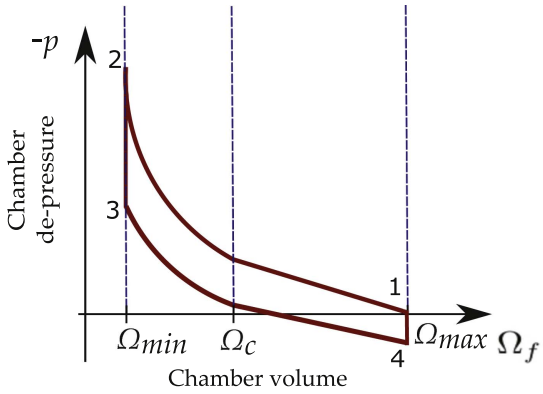

(b) De-pressure relative to ambient $-p$ (gauge) vs. fluid volume in the DFG chamber Ω_f

Figure 4. Illustrative graphs of a theoretical isopotential cycle for a DFG, whose capacitance ranges from C_l in the flat configuration and C_h in the maximal bent configuration. C_c and Ω_c refer to the 'contact' configuration, in which the membrane has only one point in contact with the plate.

dielectric materials, using the subscript f for the fluid and the subscript s for the solid, irrespective of whether it is the dielectric elastomer membrane or the rigid flat layer. In fact, the two alternatives feature the same role, as already explained in section 2.1.

If electrode curvature is neglected, the following relations hold for the electric fields in the fluid and solid layers:

$$E_f = \frac{V}{h_f + \frac{\epsilon_f}{\epsilon_s} h_s}, \quad E_s = \frac{V}{h_s + \frac{\epsilon_s}{\epsilon_f} h_f}, \tag{1}$$

where V is the voltage applied to the DFG electrodes, whereas h_f and h_s are the thicknesses of fluid and solid dielectric layers at the location of interest considered in the axial direction.

Equations (1) are obtained owing to the conservation of the electric displacement (Gauss' law) across the interface between dielectric fluid and solid:

$$\epsilon_f E_f = \epsilon_s E_s. \tag{2}$$

For the harvesting cycle at constant voltage, equations (1) highlight that the maximum electric field occurs in both solid and fluid dielectrics when the elastomeric membrane is in contact with the flat rigid electrode. In the locations of contact indeed, the thickness of both membrane and fluid are at their minima. In this condition, although in theory $h_f = 0$, the electric field across the fluid should not be neglected since, in practice, some fluid layer is always likely to remain trapped between solid dielectric and electrodes. Equation (2) indicates that the electric field is higher in the layer featuring lower dielectric constant. However, considering that the maximum value that can be supported prior to failure is material specific, the most critical layer will be the one for which the product between dielectric strength, E^{BD}, and relative permittivity, ε, is minor. This layer will be the most prone to electrical breakdown and, thus, it will set the maximum voltage bearable by the DFG.

As it will be described later, dielectric fluids are generally more critical than solids with respect to the electrical breakdown limit by virtue of their electrical properties. Different than in solids, however, electrical breakdown of fluids does not lead to instantaneous permanent failure, but only a short interruption of the functioning which make them very useful in many applications [24]. Fluids such as transformer or silicone oil are indeed known to recover rapidly and resume their insulating functions after breakdown, although some gradual degradation may occur which is likely to shorten their lifetime.

2.2.2. Limits and figures of merit. The operating limits of DFGs can be identified on the charge–voltage plane, whose characteristic curves are shown in figure 4(a). The first working limit is identified by the extremal deformations of the membrane: the flat and the fully deflected configurations correspond to minimum (C_l) and maximum (C_h) capacitance of the device, respectively (blue lines in figure 4(a)). The second working limit is identified by the maximum voltage allowed in the DFG (V_{BD}), which is caused by the breakdown of the most electrically stressed layer, i.e. the layer that reaches first its breakdown electric field.

Assuming that the fluid layer is the most stressed (see par. 2.2.3), the breakdown limit curve in the Q–V plane (green line in figure 4(a)) can be obtained by inverting the equation (1); that is

$$V_{\mathrm{BD}} = E_f^{\mathrm{BD}} \left[h_f^* + \frac{\varepsilon_f}{\varepsilon_s} (h^* - h_f^*) \right], \tag{3}$$

here h^* and h_f^* respectively indicate the thicknesses of the overall pile and of the fluid dielectric at the location (or locations) of the DFG where the the term within square brackets is minimum. Correspondingly, the breakdown limit curve in the Q–V plane is divided in two portions depending on whether the elastic membrane is in contact to the flat rigid electrode or not as shown in figure 4(a). Specifically, starting from the configuration with maximum capacitance C_h, V_{BD} remains constant as the fluid enters in the chamber and

detaches the membrane from the rigid electrode, until no point of contact will exist between them. This configuration corresponds to the DFG capacitance C_c. Beyond this configuration, fluid thickness increases everywhere in the DFG as the fluid continues entering the chamber (namely, as the DFG capacitance continues to decrease down to C_l) and thus, according to equation (3), V_{BD} can increase. Of course, variation of V_{BD} with charge is not linear since DFG capacitance does not vary linearly with the minimum thickness of the fluid layer.

In addition to the curves described above, another limit to the operation of DFG, which is however not visible in the Q–V plane, is the cycling period. In order to avoid massive charge leakage losses due to the finite resistivity of practical dielectric materials, the cycling period must be significantly lower than the discharging time constant of each layer of the stack. This will be discussed more in details in sections 2.2.3 and 4.1.

Beside the detailed representation of the functional limits in the Q–V plane, the efficacy of operation of DFGs can be summarized by the two following figures of merit: the maximum energy density that can be converted per cycle and the DFG efficiency. In order to define them, we consider the cycle obtained by performing the generating phase at the highest possible constant voltage without breakdown occurring (namely, the one with maximum energy output). This cycle overlaps the breakdown limit curve as DFG capacitance goes from C_h to C_c.

The energy balance of the system between two generic states of equilibrium is defined as

$$\mathbb{E}_m + \mathbb{E}_e = \Delta(\mathbb{U}_{\mathrm{es}} + \mathbb{U}_{\mathrm{el}}) + \mathbb{E}_l, \tag{4a}$$

where $\mathbb{E}_m$ is the mechanical work done by an hypothetical piston on the fluid entering in the chamber, $\mathbb{E}_e$ is the electrical work done by the external electrical circuit on the system, $\Delta\mathbb{U}_{\mathrm{es}}$ is the variation of electrostatic energy stored in the DFG, $\Delta\mathbb{U}_{\mathrm{el}}$ is the variation of elastic energy stored in the membrane, and $\mathbb{E}_l$ is the overall loss of energy due to dissipations.

Considering a process from i to j, where i and j are two of the generic equilibrium states of the generating cycle, equation (4*a*) can be rewritten as

$$\int_i^j p\mathrm{d}\Omega_f + \int_i^j V\mathrm{d}Q = \frac{1}{2}(C_jV_j^2 - C_iV_i^2) + \Omega_{\mathrm{el}}(\Phi_{\mathrm{el}_j} - \Phi_{\mathrm{el}_i}) + \mathbb{E}_l^{i\to j}. \tag{4b}$$

In this last equation, the first term $\mathbb{E}_m$ is given by the integral of the fluid gauge pressure p, assumed uniform within the chamber, over the volume swept by the membrane Ω_f, i.e. the volume of fluid 'moved' by the hypothetical piston, positive when entering the chamber. In the second term, V is defined as the voltage between the upper and the lower electrode and Q is the charge transferred to the DFT, positive if entering the system.

The first term on the right-hand side represents the variation of electrostatic energy of the DFG. It should be highlighted that, due to the non-constant geometry of the DFG, the value of C_j (or C_i) should be calculated as the capacitance (i.e. the ratio between charge and voltage) of a rigid capacitor whose geometry corresponds to the DFG shape in the state j (or i). As it will be shown in the experimental section, for practical values employed for the electric fields, the implemented iso-choric (i.e. constant volume of fluid) charging/discharging processes are governed by a linear relation between DFG voltage and DFG charge, i.e. $Q_{\mathrm{DFG}}/V_{\mathrm{DFG}} = C$ is constant. As a consequence, in the following C is treated as the (constant) iso-choric capacitance of the whole system, measured between the electrodes. Thus, the electrostatic energy can be practically calculated as in equation (4*b*). According to the previous hypotheses, if the shape of the deflected membrane is known, C can be evaluated, as an approximation, by the integral over the flat rigid electrode surface, S, of the infinitesimal capacitance of the dielectric layers stack

$$C = \int_S \left(\frac{h_s}{\epsilon_s} + \frac{h_f}{\epsilon_f}\right)^{-1} \mathrm{d}S. \tag{5}$$

In the fourth term, Ω_{el} is the constant volume of the deformable dielectric elastomer membrane and Φ_{el_j} (or Φ_{el_i}) is the average of the volumetric elastic energy density of the elastomeric material the membrane is made of. Φ_{el} can be calculated by the integration of a hyper-elastic energy density function, as defined by Ogden [25], over the membrane volume, where local strains are known or assumed.

Fluid viscous dissipation, elastomer mechanical losses due to inelasticities and charge leakage losses are included in the term $\mathbb{E}_l^{i\to j}$, as well as the resistive electrical losses that occur in the electrodes.

For a complete harvesting cycle at constant voltage V, like the one depicted in figure 4(a), the electrical energy that can be theoretically generated in absence of dissipations is

$$\mathbb{E}_{e,T} = (C_3 - C_4)\frac{V^2}{2}. \tag{6}$$

For a given DFG, equation (6) highlights that $\mathbb{E}_{e,T}$ will be larger as the capacitance at system discharge, C_4, is made smaller. For this reason, in DFTs the capacitance ratio, C_3/C_4, is a figure significantly higher than in other existing MVC devices. Since in real DFG, this figure can be larger than 15 (as in the prototype described in section 3.1), for preliminary calculations the following simplification can be made

$$\mathbb{E}_{e,T} \cong C_3\frac{V^2}{2}. \tag{7}$$

Equation (7) highlights that, for the cycle executed at constant voltage, the harvested energy can be nearly equal to the priming energy required for system activation. Besides, since the membrane adheres totally to the flat electrode,

$$C_3 = \epsilon_s\Omega_{\mathrm{el}}/h_{s,3}^2 \tag{8a}$$

and

$$V = E_{s,3}\, h_{s,3}, \tag{8b}$$

where $h_{s,3}$ and $E_{s,3}$ indicate the thickness and the electric field of the dielectric elastomer membrane at state 3, and equation (7) can also be rewritten as

$$\mathbb{E}_{e,T} \cong \epsilon_s \Omega_{\mathrm{el}} \frac{E_{s,3}^2}{2} = \epsilon_s \Omega_{\mathrm{el}} \frac{V^2}{2h_{s,3}^2}. \tag{9}$$

By virtue of equation (2), equations (8*b*) and (9) also read as

$$\mathbb{E}_{e,T} \cong \Omega_{\mathrm{el}} \frac{D_{f,3}^2}{2\epsilon_s}, \tag{10}$$

where $D_{f,3}$ indicates the electric displacement field ($D_{f,3} = \epsilon_f E_{f,3} = \epsilon_s E_{s,3}$) in the infinitesimal fluid layer that may be trapped between dielectric elastomer and electrodes in state 3. As already mentioned in section 2.2.1, considering that the electric fields in either the solid or the fluid layer cannot be larger than the dielectric strength of the respective material, equations (9) and (10) can be used to estimate the maximum electrical energy that can be generated by the DFG in a harvesting cycle executed at constant voltage. In particular, if the fluid is the weaker dielectric, the following upper limit can be defined for the DFG energy density (namely, the energy that can be harvested by the DFG for a unit volume of the employed dielectric elastomer material)

$$\frac{\mathbb{E}_{e,T}}{\Omega_{\mathrm{el}}} < \frac{(\epsilon_f E_f^{\mathrm{BD}})^2}{2\epsilon_s}. \tag{11}$$

The electrical energy given by equation (6) is a strictly theoretical value. In practice, mainly due to charge leakages between the electrodes (which is a consequence of the finite resistivity of real dielectrics), the true electrical energy, $\mathbb{E}_e$, that can be extracted by a practical DFG will be smaller (namely, $\mathbb{E}_e < \mathbb{E}_{e,T}$). In the absence of mechanical dissipation, considering the cycle of figure 4, $\mathbb{E}_{e,T}$ will equate the mechanical work, $\mathbb{E}_{m,T}$ performed by the fluid over the entire harvesting cycle. However, due non-negligible viscosity of real elastomers and fluids, $\mathbb{E}_{m,T}$, will be smaller than the true mechanical work, $\mathbb{E}_m$, performed by the fluid over the entire cycle; that is:

$$\mathbb{E}_m = \int p \mathrm{d}\Omega_f > \mathbb{E}_{m,T} = \mathbb{E}_{e,T} > \mathbb{E}_e. \tag{12}$$

On account of equation (12) , the efficiency of a practical DFG can then be defined as

$$\eta = \frac{\mathbb{E}_e}{\mathbb{E}_m}. \tag{13}$$

2.2.3. Materials. In this paragraph we discuss influential parameters for DFG's design. As already mentioned in previous sections, the product between fluid relative permittivity and its dielectric strength $\epsilon_f E_f^{\mathrm{BD}}$ is a key parameter for the prediction of DFGs performance. This value corresponds to the maximum displacement field D^{BD} that the materials can withstand before electrical breakdown occurs and, as shown by equation (11), the maximum DFG energy density depends on its second power law.

If the fluid is the weaker dielectric, equation (11) also shows that a high permittivity of the elastomer membrane decreases the energy density of the DFG, although, according to equation (9), it may lower the operating voltage, while maintaining acceptable performances. The addiction of an extra solid dielectric layer, thus, could be a reasonable compromise in case of strict voltage specifications.

Since real dielectrics always feature finite electrical resistivity, DFGs are affected by charge leakage from one electrode to the other. In order to limit leakage losses, the cycle execution time must be significantly faster than the typical discharge time, $\tau_k = \rho_k \epsilon_k$, of each kth dielectric material within the stack (where ρ_k is its electrical resistivity). Moreover, if the characteristic discharge times between two adjacent dielectric layers are significantly different, an electrostatic surface charge may accumulate on the interface [26], which can be calculated with the relation

$$\sigma_c = \frac{V}{R_t h_t}(\tau_s - \tau_f), \tag{14}$$

where σ_c is the charge density on the contact interface at steady conditions, R_t and h_t are the overall resistance and height of the dielectric stack, V is the overall voltage across the stack, τ_s and τ_f are, respectively, the discharge constants of the solid and fluid dielectric layers. This surface charge shall be avoided, since it may lead to transient leakage phenomena that are arduous to predict.

The typical electrical parameters of some materials of potential interests for the implementation of DFGs are summarized in table 1. The considered solids for the deformable membrane are natural, synthetic, silicone and acrylic rubbers. Rigid mica and glass are also listed for the implementation of DFG architectures that require a stiff solid dielectric as those described in section 2.1 and schematized in figure 2. The considered fluids are mineral/silicone oils and insulating esters that are of widespread use in the transformers insulation industry. Such fluids are designed to have large dielectric strength; however, their electrical permittivity is limited since this property is not of great interest for their target application.

The considered parameters have been collected from commercial data-sheets. When dielectric strength values were given as the result of a sphere-to-plane test, a non-uniformity factor equal to 1.5 has been applied to convert the value to the plane-to-plane scenario instead [27].

Preliminary chemical compatibility between commercially available elastomers and fluids has been checked through a visual contact test: a drop of fluid has been left on the elastomer surface for 24 h and eventual effects have been recorded. From results shown in table 2, we can assume that silicone oil is compatible with all tested elastomers, except for silicone rubber. Moreover, the acrylic elastomer is found to adsorb both mineral oil and ester with visible effects on a 24 h timescale. The ester is efficient in chemical compatibility, but

Table 1. Relevant electrical properties of materials that could be employed for the manufacturing of compliant and fluid layers of DFGs. [22, 23, 27].

	Material	Relative permittivity ε_r	Dielectric strength E^{BD} (MV m^{-1})	Breakdown disp. field $D^{BD}/\epsilon_0 = \varepsilon_r E^{BD}$ (MV m^{-1})	Electrical resistivity ρ (Ω m)	Discharge constant $\tau = \rho \epsilon$ (s)
Fluid	Silicone oil	2.7	30–45	81–121	10^{13}	23.9
	Mineral oil	2.2	39	86	10^{11}	1.9
	Ester	3.2	45	144	3×10^{10}	0.8
Elastomer	Natural rubber	2.7	100–300	270–810	10^{12}	23.9
	Synthetic rubber	2.7	100–300	270–810	2×10^{12}	47.8
	Silicone rubber	1.5–2.8	70–150	105–420	10^{12}	13.3
	Acrylic rubber	2.9–4.1	60–180	168–738	2×10^{11}	2.6
Solid Layer	Mica	3.0–6.0	118	354–708	10^{13}	265.5
	Glass (Pyrex)	3.7–10.0	9.8–13.8	36–138	10^{12}	32.7

Table 2. Summary of the preliminary test of chemical/physical compatibility between dielectric fluids and dielectric elastomers.

Elastomer	Fluid		
	Silicone oil Xiameter 200 50st	Mineral oil IP Ditrans CK	Ester MIDEL 7131
Synthetic Theraband	*Effects:* none *Usable:* YES[a]	*Effects:* chem. or phys. alterations *Usable:* NO	*Effects:* chem. or phys. alterations *Usable:* NO
Natural rubber Oppoband	*Effects:* none *Usable:* YES[a]	*Effects:* chem. or phys. alterations *Usable:* NO	*Effects:* chem. or phys. alterations *Usable:* NO
Silicone Elastosil wacker	*Effects:* chem. or phys. alterations *Usable:* NO	*Effects:* chem. or phys. alterations *Usable:* NO	*Effects:* none *Usable:* YES[a]
Acrylic VHB 3M	*Effects:* none *Usable:* YES[a]	*Effects*: minor/slow interaction *Usable:* uncertain	*Effects:* minor/slow interaction *Usable:* uncertain

[a] Potential usability for DFG is predicted on the basis of these interaction tests, further investigations should be conducted to better asses viability and performance.

it features a small discharge constant which may limit the energy generation efficiency in most practical applications. This has been verified via additional generation tests—not disclosed in this paper—that showed significant leakage losses in the frequency range $0.1 \div 1$ Hz.

In conclusion, among the considered fluids, silicone oil results the best option to trade-off between electrical properties and compatibility with some of the most common elastomers. Development and adoption of dielectric fluids appositely conceived for DFG application, should be considered in the near future.

3. Experimental

3.1. Prototype

This section describes a prototype built to provide an experimental proof of the DFG concept. Despite this device is a first unoptimized demonstrator that leaves large room for future improvements, it is already well behaved and demonstrates the most important aspects of system operation and performances.

A schematic and a picture of the test bench are shown in figures 5 and 6, respectively; it comprises the DFG prototype, a hydraulic sub-system, a high-voltage (HV) electronics sub-system and a real-time controller. Specific details for each sub-system are provided below.

The DFG prototype: that is considered for experimental implementation is built according to the cCFr topology (see figure 2). This consists in a fluid chamber confined at the bottom by a rigid brass plate, laterally by an annular fluid distributor made in ABS, and at the top by a dielectric elastomer membrane, which is held by an ABS ring-shaped support. These ABS components are manufactured with 3D-printing process and parts were exposed to acetone vapors and subsequently dried in order to ensure waterproofing. A cross-section rendering of the device is shown in figure 7(a).

The fluid chamber is filled with Xiameter® PMX-200 50 CS, a dielectric silicone oil, that was tested in combination with DET to provide enhanced electrical performances [28].

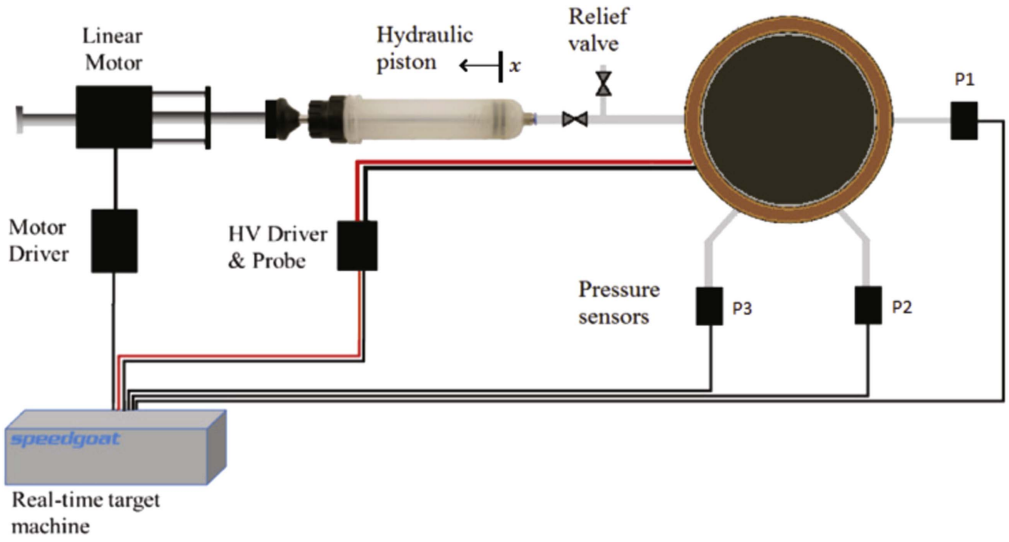

Figure 5. Scheme of the test-bench used with the first DFG prototype. The DFG is connected to a hydraulic piston that is driven by a linear electric motor to control the volume of displaced fluid; a high voltage (HV) driver is employed for the electrical activation and three pressure sensors are monitoring the pressure in the fluid chamber. The whole system is controlled by a real-time target machine.

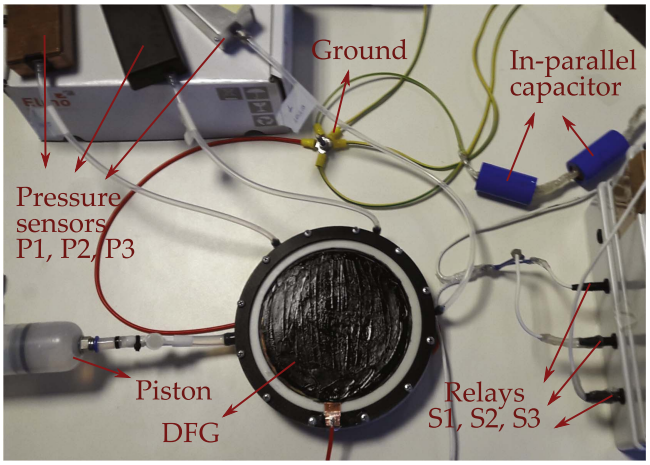

Figure 6. Picture of the test-bench which shows: the DFG prototype (bottom-center); the hydraulic piston (partially shown on the left); components of the HV circuitry (the relays box and in-parallel capacitors on the right); the pressure sensors connected to the chamber through standard pneumatic piping (on the top-left); the star-grounding connection (top-center).

The annular distributor body serves: (1) to convey the fluid that is injected from an inlet-outlet duct into a uniform radial flux toward the center of the chamber; (2) to hold the membrane-support at constant distance from the brass plate; (3) to provide three side openings, arranged with an angular distance of 60°, for pressure sensing. The brass plate is bonded to the distributor using an acrylic sealant; at the top, the sealing is guaranteed by the membrane itself. External flanges and screws—not shown in the figure—hold the device firmly and assure oil-tightness.

The structure of the upper elastomeric membrane is obtained by gluing together three layers (0.5 mm each before stretch) of a commercial double-sided pressure-sensitive acrylic tape VHB 4905 by 3M and is stretched onto the ring-shaped support. Using a common/simple solution for the implementation of deformable electrodes [29], the upper side of the membrane is painted with a carbon conductive grease (MG-Chemicals 846).

The internal diameter of the ring as well as the brass plate is $d = 150$ mm and the distance between the electrodes in the flat position is $h = 4.5$ mm. The membrane is fixed to the ring-shaped support after being pre-stretched to a value of $\lambda_p = 3.0$. The value of such pre-stretch is rather important for the operation of the prototype. Pre-stretch generates the needed pre-stress that makes it possible for the dielectric elastomer to smoothly detach from the brass electrode during the generation phase (i.e. when the fluid is impinged into the transducer). Such a pre-stretch has been chosen through a series of preliminary tests with progressively increasing magnitudes. This value results the minimum that guarantees a smooth operation of the device during the generation phase. Lower values cause an undesired behavior, delaying the detachment of the membrane. It is worth noting that stretches up to $\lambda = 1.12$ are applied during the operation, leading to a possible maximum value of total stetch of $\lambda_t = \lambda\lambda_p = 3.36$, largely below the rupture limits for VHB material [30, 31]. However, the employment of stiffer elastomeric dielectric materials might make it possible to widely reduce the pre-stretch level.

Considering relative permittivities of $\varepsilon_f = 2.7$ and $\varepsilon_s = 4.15$ for silicon oil and acrylic elastomer respectively, the expected minimum and maximum capacitance of this prototype are $C_l = 92.0$ pF and $C_h = 2.34$ nF. The minimum capacitance is obtained assuming a completely flat membrane, while the maximum capacitance is obtained introducing an assumption on the deformed shape of the membrane in the configuration with minimum amount of dielectric oil. The assumed geometry, shown in figure 7(b), features a flat shape for the part of membrane in contact with the brass electrode and a toroidal shape for the part of membrane that is not in contact with the electrode, i.e. the part of membrane detached

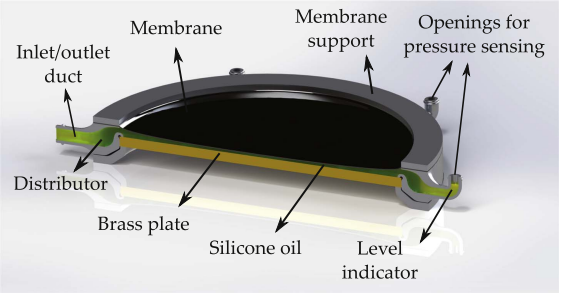

(a) *Scheme of a cross section of the DFG prototype.*

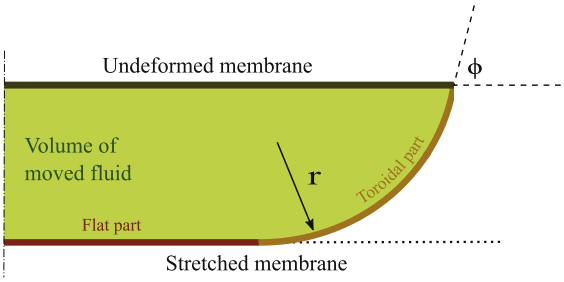

(b) *Scheme of the geometry assumed for the capacitance calculation.*

Figure 7. CAD drawing of the DFG prototype with labeled components (a) and scheme of the toroidal geometry that has been chosen for calculating the equivalent capacitance of the non-flat part of the DFG (b).

is assumed to have a constant curvature radius on the meridian cross section and is connected to the flat part through a horizontal tangent. Given this geometry and considering a maximum fluid volume displacement of $\Omega_f = 67.1\ \mathrm{cm}^3$, the membrane shape is completely defined and the capacitance can be calculated in an approximated way via equation (5). According to this calculations, the contribution of the membrane part that is in contact with the brass electrode accounts for 86% of the total, i.e. it is much more relevant with respect to the remaining toroidal part.

According to equation (6), introducing the dielectric strength $E_f^{\mathrm{BD}} = 45\ \mathrm{MV\ m^{-1}}$ for the fluid, and keeping the parameters and the expected capacities considered above, the estimated maximum theoretical electrical output is $\hat{\mathbb{E}}_{e,T} = 17.98\ \mathrm{mJ}$ per cycle .

Hydraulic sub-system: to feed oil into and out of the device, a hydraulic system has been connected to the DFG prototype. This is composed by an oil syringe (E200-907 by Expert-tool) actuated via a brushless linear motor (P01-37 × 120F/200 × 280-HP by LinMot). The system provides accurate control of piston position x thanks to a closed loop feedback controller implemented in the motor driver.

To vent air from the hydraulic system, a relief valve is mounted on the inlet/outlet duct. The connections between the prototype, the syringe and the valves are made with semi-flexible silicone pipes with 7 mm internal diameter. The three pressure sensors $P1$, $P2$ and $P3$ are connected to the DFG side openings throughout thinner silicone pipes, which allow for a small air buffer. Each sensor measures a differential oil pressure with reference to the one evaluated at the beginning of each test.

3.2. Electronics and control

In order to provide an accurate control of the system according to the cycle of generation and to obtain an accurate estimation of the overall energy produced per cycle, a custom high voltage circuit has been developed.

HV electronics sub-system: The circuit of the custom made HV driving electronics developed to control DFG charge and discharge, is represented in figure 8. It comprises a HV power amplifier (Trek Model 10/10B-HS), which regulates the voltage V_d, and three HV reed relays (H24-1A69 by

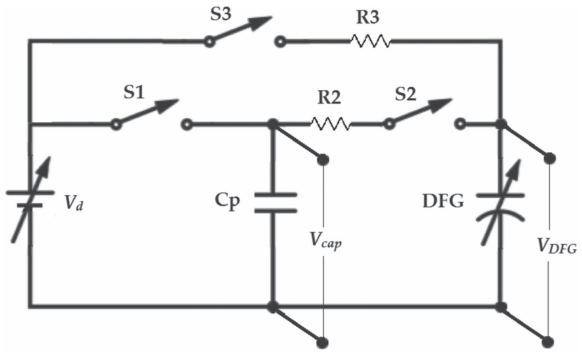

Figure 8. High voltage circuit implemented in the generation test. V_d is the voltage imposed by the HV driver, while V_{cap} and V_{DFG} are measured by HV probes.

MEDER electronic) that alternatively connect the DFG electrodes to either the power amplifier or an in-parallel capacitor $Cp = 23.5\ \mathrm{nF}$ (obtained as a series of two 47 nF HV capacitors as indicated in figure 6).

A resistor $R3 = 1\ \mathrm{M\,\Omega}$ is used to fully discharge the DFG through the power amplifier as the relay S3 is closed, whereas resistor $R2 = 1\ \mathrm{M\,\Omega}$ is used to limit the peak current that occurs during DFG priming to the instrumentation limit of 5 mA, as the relay $S2$ is closed. To measure the voltage V_{DFG} across the DFG electrodes, as described in [32], a custom made HV probe has been implemented that features large bandwidth and very high input resistance (nearly 100 G Ω), which drastically limits the drain of charge from the DFG electrodes. In order to minimize the current leakage of the power electronics, all the HV wirings and components have been encapsulated via thick layers of acrylic tape (VHB 4905 by 3M).

Real-time controller sub-system: A real-time machine (Performance real-time target machine by SpeedGoat) running the MatLab xPC Target software environment is employed to control both motion of the piston and charging status of the DFG [33]. This set-up enables to command any complex profile for piston position x, and DFG voltage V_{DFG}. In this work, the position of the piston is simply controlled according to programmed constant-speed trajectories with different durations, whereas V_{cap}, and subsequently V_{DFG}, is

controlled according to a particular energy harvesting cycle, using different values of voltage target, which are called V_{in}.

The harvesting cycle used in this experiment closely resembles the one described in [10]. It uses the capacitor C_p placed in parallel to the DFG so as to transfer charge in both priming and generating phases. The higher is the parallel capacitance with regard to that of the DFG, the more this cycle approximates the constant voltage cycle described in section 2.2.1.

Specifically, the voltage V_d commanded by the power amplifier and the reed relays run according to the following sequence of operations.

(i) Capacitance Increase:
- $S1$ and $S2$ are opened, $S3$ is closed;
- the voltage of the driver is set to $V_d = 0$, i.e. $V_{\text{DFG}} = 0$;
- the fluid is drawn out of the chamber with flow rate $\mathcal{Q}_{\text{out}}$, i.e. DFG capacitance is increased ($1 \rightarrow 2$) until the piston has undergone the largest displacement.

(ii) Priming:
- the position of the piston is kept fixed;
- $S3$ is opened, i.e. the DFG is isolated, and $S1$ is closed;
- the capacitor C_p is charged, with a voltage supply $V_d = V_{\text{in}}$.
- C_p is disconnected by opening $S1$;
- the switch $S2$ is closed, thus the DFG is rapidly charged ($2 \rightarrow 3$) connecting it to C_p.

(iii) Generation:
- the DFG and the capacitor are kept connected (in parallel);
- the piston returns to its initial position according to a flow rate $\mathcal{Q}_{\text{in}}$; the membrane thus reaches the flat configuration ($3 \rightarrow 4$), corresponding to the state where DFG exhibit minimal capacitance.

(iv) Discharge:
- the position of the piston is kept fixed;
- the DFG is isolated by opening $S2$;
- $S3$ is closed and the DFG is discharged to ground ($4 \rightarrow 1$).

Triggering within the sequences (ii), (iii) and (v), is obtained by switching two reed relays with a fixed time distance equaling 0.03 s. At the end of sequences (ii) and (iv), a wait time of 1 s has been introduced to allow for the membrane adjustment.

4. Test and results

4.1. Data acquisition and processing

The demonstration of the effectiveness of DFT at a proof-of-concept level has been performed by two series of generation tests, both conducted with the procedure presented in the previous section, plus a repeatability test.

Each test consists of two generation cycles in which the membrane moves from a flat position to the maximum deflected one. For each cycle, the piston starts from the rest position where the membrane is flat, moves back until the membrane is fully deflected and than returns to its initial position. Capacitor's voltage V_{cap}, DFG's voltage V_{DFG} and three pressure signals $P1$, $P2$, $P3$ were recorded throughout the test with a 10 kHz sampling rate. All the signals were filtered and re-sampled to 500 Hz for noise reduction. An example of resulting data for one cycle with parameters $V_{\text{in}} = 4$ kV, $\mathcal{Q}_{\text{out}} = 16$ cm^3 s^{-1}, $\mathcal{Q}_{\text{in}} = 72$ cm^3 s^{-1} is shown in figure 9.

The first series of experiments was performed for different values of the imposed voltage V_{in} in the range $0.5 \div 5.5$ kV, by increasing the target voltage by 0.5 kV for each successive test (for $\mathcal{Q}_{\text{out}} = 16$ cm^3 s^{-1} and $\mathcal{Q}_{\text{in}} = 80$ cm^3 s^{-1}). The second series of experiments explores the dependency of system performance on the input flow rate in the range $16 \div 72$ cm^3 s^{-1} (all tests performed with $\mathcal{Q}_{\text{out}} = 16$ cm^3 s^{-1} and $V_{\text{in}} = 4$ kV) namely, by executing harvesting cycles with different durations of the generation phase. Lastly, a test with 10 consecutive harvesting cycles is conducted to explore repeatability of system performance. After experiments, acquired data have been manipulated to calculate the net generated energy and mechanical work input and efficiency.

The net energy generated can been estimated according to the following relation

$$\mathbb{E}_e = \int_2^3 V_{\text{DFG}}\,\mathrm{d}Q_{\text{DFG}} + \int_3^4 V_{\text{cap}}\,\mathrm{d}Q_{\text{cap}} + \int_4^1 V_{\text{DFG}}\,\mathrm{d}Q_{\text{DFG}}. \tag{15}$$

Equation (15) is obtained by summing three terms: the first, which is negative, is the electrical energy transferred to the DFG during the priming phase, i.e. the energy input used to charge the DFG; the second is the energy transferred from the DFG to the capacitor during the generating phase, i.e. an electrical energy output; the third is the energy transferred to the ground during the discharging phase, i.e. another electrical energy output.

Such integral terms can be calculated as follows. The evaluation of second term is rather straightforward since the relation $Q_{\text{cap}} - V_{\text{cap}}$ can be assumed as linear since the capacitance of C_p is constant. The computation of the first and last integral terms, corresponding to priming and discharging phases, can be more complex, since the relation $Q_{\text{DFG}} - V_{\text{DFG}}$ is generally nonlinear for a variable capacitor [34]. In order to evaluate this effect, we have characterized the $Q_{\text{DFG}} - V_{\text{DFG}}$ relation, running experiments with increasing voltages (see figures 10 and 11). As it can be observed, the $Q_{\text{DFG}} - V_{\text{DFG}}$ relation can be assumed as linear. This means that the DFT exhibits a constant capacitance in both the isochoric (null flow rate) transformations that correspond to priming and discharging phases.

According to these assumptions, equation (15) is simplified to

$$\mathbb{E}_e = -\frac{1}{2}C_h\,V_3^2 + \frac{1}{2}C_p\,(V_4^2 - V_3^2) + \frac{1}{2}C_l V_4^2, \tag{16}$$

that is lastly used for the evaluation of the energy generated during the experiments.

The contributes of the different terms of equation (15) can be visualized in figure 10. In figure 10(a) the red area

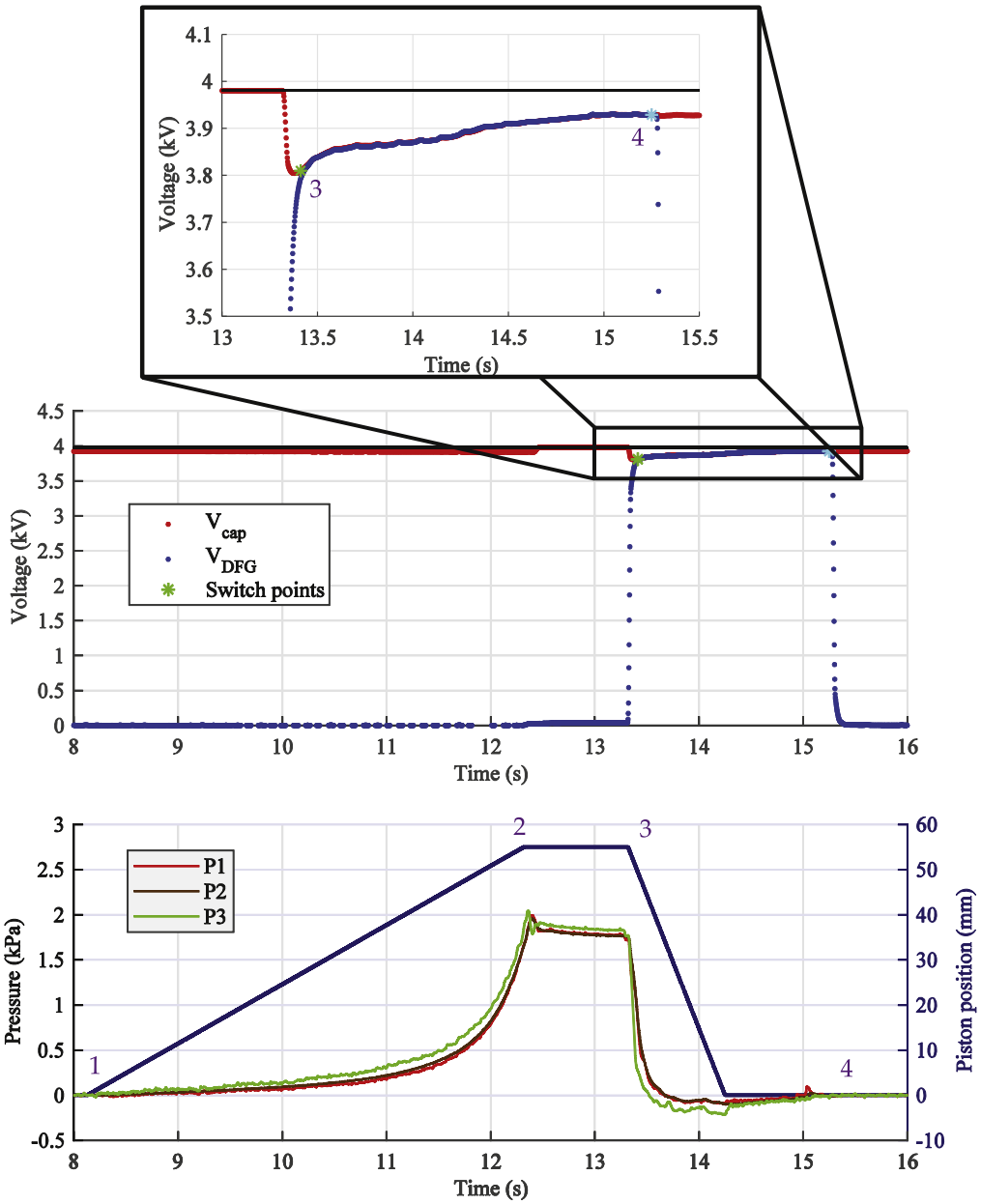

Figure 9. Voltage and pressure measures in a generation test with $V_{in} = 4$ kV, $Q_{out} = 16$ cm^3 s^{-1} and $Q_{in} = 72$ cm^3 s^{-1}. In the upper plot, red dyed is the capacitor voltage V_{cap}; blue dyed is the DFG voltage V_{DFG}. In the lower plot, blue dyed is the target piston position x; red, brown and green dyed are the gauge de-pressure $-p$, by sensors $P1$, $P2$ and $P3$, respectively.

represents the priming energy, while the blue area is the energy left in the DFT at the end of the generating phase; in figure 10(b) the green area is the energy transferred to the capacitor during the generation phase. These last two terms (blue and green areas) are considered as an estimate of the harvested energy, even if they are ultimately dissipated at the end of each cycle. This is purposely done because the test-bench is not able to store energy between one cycle and the following one. The energy generated across the whole cycle $\mathbb{E}_e$ is finally calculated as the algebraic sum of harvested energy and priming energy.

As regards the capacitance values C_l and C_h that are required in equation (16), they have been estimated through independent measurements at increasing voltages while the inflation level was kept constant in the two corresponding positions.

Obtained values are $C_h = 1.09$ nF and $C_l = 83.5$ pF, that are smaller than the expected theoretical values of 2.34 nF and 92.00 pF reported in section 3.1. The significant discrepancy on C_h is probably attributed to an amount of fluid that remains trapped between the rigid electrode and the elastomeric dielectric. Due to this difference the maximum theoretical electrical output of 17.98 mJ mentioned in section 3.1 needs to be downgraded to 7.9 mJ per cycle.

Processed data from the series of experiments at different voltage are shown in the Q–V plots of figure 11, where the charge on the DFG at the end of the priming and generating phases are respectively calculated as $Q_3 = C_p(V_2 - V_3)$ (red

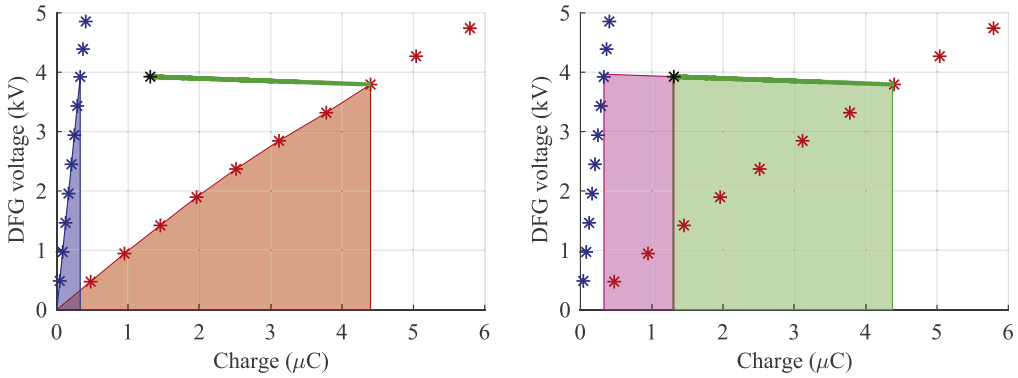

(a) *Priming and discharging phase.* (b) *Generating phase.*

Figure 10. Graphic representation of the energy transferred to the DFG during the priming phase (light red), to the capacitor in the generating phase (green) and from the DFG in the discharging phase (blue). In deep red is represented the energy lost due to leakages.

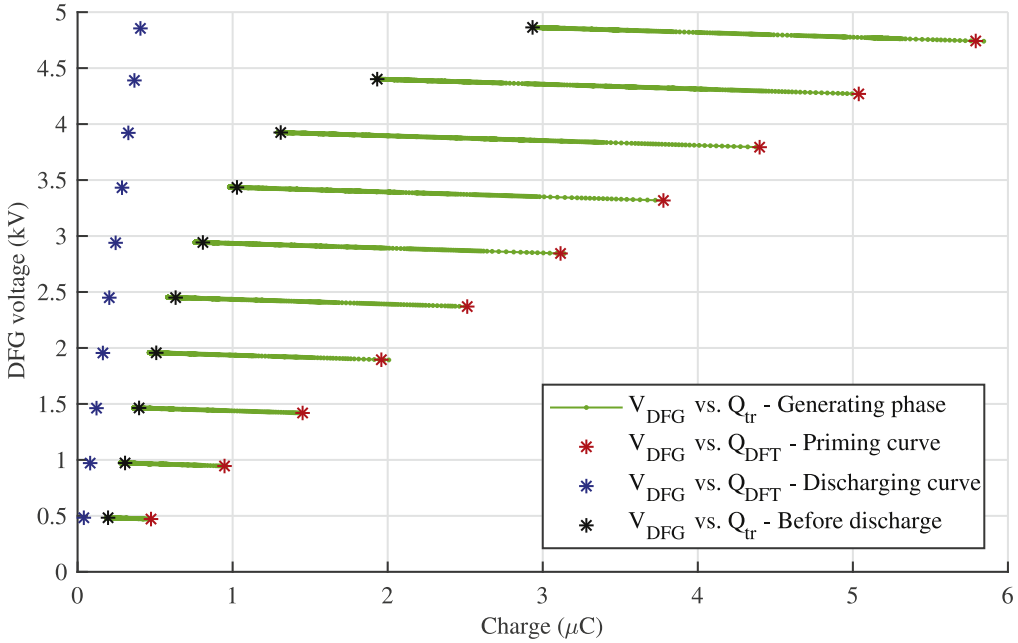

Figure 11. Results at raising input voltages for $\mathcal{Q}_{out} = 16\ cm^3\ s^{-1}$ and $\mathcal{Q}_{in} = 72\ cm^3\ s^{-1}$. The red asterisks shows the characterization of the priming curve; green dyed is V_{DFG} versus Q_{tr} i.e. the generating curve comprehensive of charge leakages; the blue asterisks shows the characterization of the discharging curve; The black asterisks are determined by the charge that is transferred to C_p at the end of the generating phase. Refer to equation (16) for a deeper interpretation of the graph.

asterisks) and $Q_4 = C_l\ V_4$ (blue asterisks), while the charge transferred to C_p during the generation phase is calculated as $Q_{tr} = C_p(V_4 - V_3)$.

It is worth to notice that in absence of charge leakages $Q_4 = Q_3 - Q_{tr}$, while in practice, differences are observed as shown by the different position of black and blue asterisks in figure 11. Energy losses related such leakages can be visualized looking at the corresponding modification of area under the green lines that represents the net energy transferred to the capacitor C_p during the generating phase. In particular, leakage losses related to the generation phase can be calculated subtracting the energy generated in a theoretically leakage-free cycle and the real generated energy. A leakage free-cycle would have brought to an increased value of the voltage V_4. Such a theoretical value can be calculated through charge conservation. The energy losses due to leakages can be then estimated and are represented in the deep red area in figure 10(b).

The mechanical work input to the DFG over the entire energy generation cycle has been estimated through the numerical integration of chamber pressure over the fluid volume displaced by the syringe, as for equation (12). Calculation has been performed by considering as the chamber pressure the average of the three measurements made by sensors $P1$, $P2$ and $P3$.

Except for the tests performed at the highest flow rates, discrepancies between the three sensors $P1$, $P2$ and $P3$ were significantly little with respect to the overall pressure

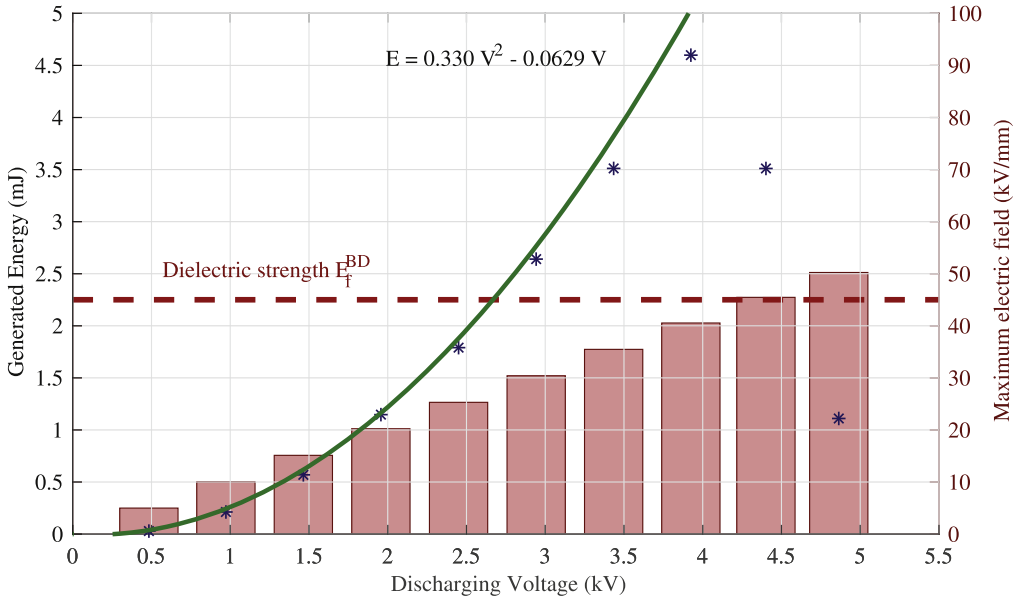

Figure 12. Estimated generated energy plot (blue asterisks) against the priming voltage of the DFG. The interpolation (green continuous line) highlights a quadratic dependence on voltage. The corresponding magnitude of electric field in the dielectric fluid is shown by the red bar-plot. All tests are conducted with flow rates $Q_{out} = 16\ cm^3\ s^{-1}$ and $Q_{in} = 72\ cm^3\ s^{-1}$.

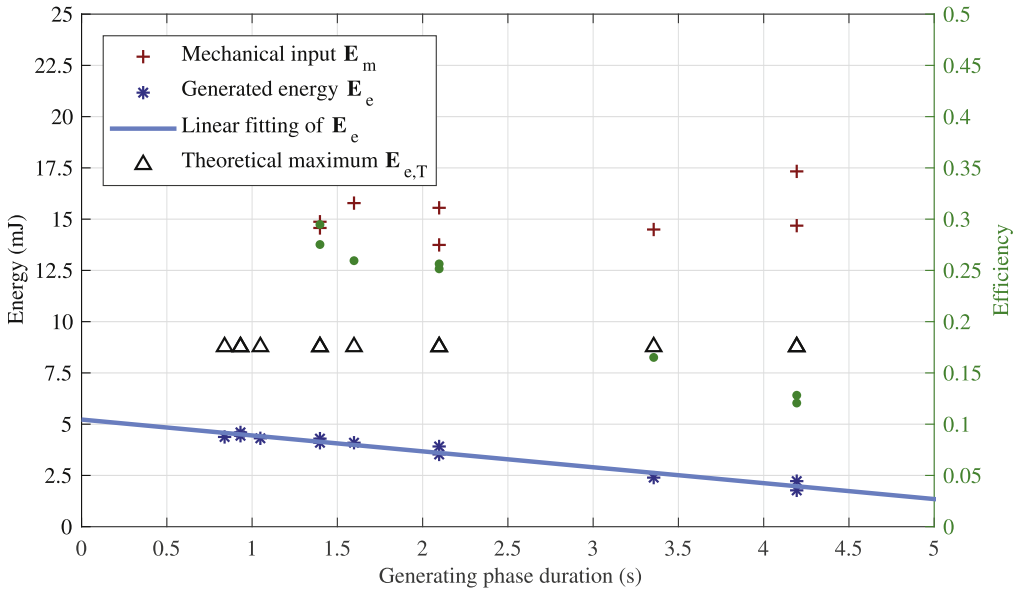

Figure 13. Estimate of converted energy, theoretical maximum energy that can be converted and efficiency (green dot markers) of the DFG, over the duration of the generating phase. $V_{in} = 4$ kV, $Q_{out} = 16\ cm^3\ s^{-1}$, Q_{in} ranges between 16 and 80 $cm^3\ s^{-1}$.

variation, therefore the average of the three measures has been deemed reliable as chamber pressure estimate. Mechanical work calculation has not been performed only for inlet flow rates Q_{in} higher than $50\ cm^3\ s^{-1}$, because above this speed significant fluid dynamic effects took place which reduced pressure uniformity and, consequently, made the chamber pressure estimation unreliable. Upon having calculated the net generated energy and the mechanical work input per cycle, DFG efficiency has been estimated according to equation (13). Results are presented and discussed in details in the next section.

4.2. Results and observations

A summary of the results obtained during the tests conducted with different imposed priminging voltages and different output fluid flow rates is reported in figures 12 and 13, respectively. In particular, figure 12 reports the energy harvested per cycle as a function of the priming voltage. As shown, in the lower voltage range, a parabolic interpolation shows excellent data fitting, as expected by equation (7). The converted energy per cycle follows such a quadratic behavior up a voltage of 4 kV, where a maximum of 4.6 mJ for the

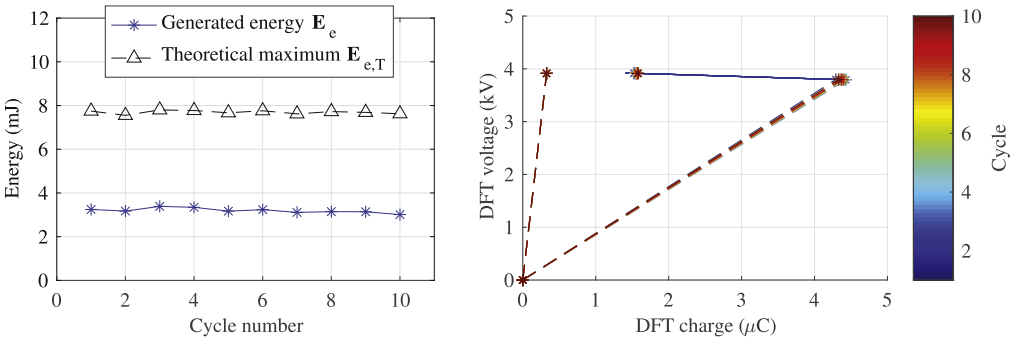

(a) *Generated energy.* (b) *Charge vs. Voltage graph.*

Figure 14. Results of the repeatability test. $V_{in} = 4$ kV, $\mathcal{Q}_{out} = 16$ cm^3 s^{-1}, $\mathcal{Q}_{in} = 72$ cm^3 s^{-1}. Figure 14(a) shows a substantially constant energy generated in consecutive cycles. In figure14(b) the main elements of the graphical representation of the generated energy are represented for each cycle.

converted energy is recorded. With the further increase in the priming voltage, there is a clear degradation in the performances that can be attributable to an increased level of charge leakages. As highlighted in the figure, the voltage value at which degradations are starting is consistent with the theoretical breakdown limit of the silicone oil layer.

Figure 13 reports the dependency of the converted energy on the duration of the generation phase for cycles performed with an activation voltage of 4 kV. As shown, for other similar operating conditions, the amount of energy that can be harvested by the DFG increases as the generating phase is performed faster, with the dependency being almost linear. This linear relationship may be the consequence of a constant rate of charge losses, due to leakages through both the fluid and the elastomer dielectrics. In fact, the shortening of generating phase allows for less charge to be dissipated through them. These results highlight that reducing the cycle period may be a good strategy to improve DFG efficiency. More than this, the linear interpolation shows a potential value of 5.2 mJ for the energy that can be converted, for very fast rates. As it can be seen, this value is about 66% the theoretical value of 7.9 mJ that, as described in section 4.1, can be estimated via equation (6) by using the experimentally measured values of the capacitances C_l and C_h.

It is worth noting that this consideration is not taking into account the effect of mechanical losses due to fluid viscosity and to inelastic response of the elastomeric membrane. An esteem of their incidence can be inferred from the difference $\mathbb{E}_m - \mathbb{E}_{e,T}$ (see figure 13), i.e. the quantity which represents the difference between the mechanical input energy and the theoretical electrical output of an ideal cycle featuring an equal capacitance variation. In percentage with respect to the mechanical energy input, these losses amount to an average of 39.7%.

Since this manuscript is intended to be just a proof of the DFT concept, optimization of mechanical losses is not treated in depth. However, we expect that a large margin of improvement of this figures can be obtained through an improved fluid-dynamic design and the employment of elastomers that possess a response closer to a perfectly elastic solid.

In addition to showing converted energy, for the slowest cycle rates, figure 13 also reports the calculated mechanical work input (red cross markers) and the efficiency (green dot markers) of the considered DFG. As expected, efficiency also increases as the generating phase is performed faster and exhibits a maximum of up to 30%. Finally, figure 14 shows the repeatability of system behavior across consecutive cycles performed with an activation voltage of 4 kV. In this multi-cycle test the amount of generated energy is rather consistent over the different iterations and makes it possible to estimate an average power output of 0.575 mW for the cycles with fastest flow rate.

5. Conclusions

This work introduces the novel concept of DFTs and proves their working principle via both experimental and theoretical considerations. These new transducers are variable capacitors, realized with a dielectric fluid, different dielectric materials such as elastomers, and variable-geometry electrodes. When used as generators, they are able to convert oscillating pressures into electrical energy. In addition to the presentation of the concept, some figures of merit to estimate system performance have also been introduced and some of the most promising architectures for its physical implementation have been described.

The importance of the dielectric fluid electrical properties has been outlined, both by theoretical and experimental considerations. In order to reach the best performances, the fluid requires a large product between permittivity and breakdown field, as well as a high electrical resistivity. A preliminary analysis of commercially available materials for system implementation has been performed finding the best available solution in the combination of a silicone oil and an acrylic elastomer. In addition to chemical compatibility, this combination features good values of electrical properties for both the fluid and the elastomer.

Using these materials, a proof of concept of DFG device has been developed and tested. Despite its preliminary design, the device already shows extremely promising performances

including: a conversion efficiencies of up to 30% and converted energy densities of 63.8 mJ g^{-1} and 173 mJ cm^{-3} per cycle, referred to the employed silicone oil and acrylic elastomer, respectively. These figures of merit have been proved to be repeatable over a sequence of multiple cycles of operation.

Beside these promising results, the most interesting aspect of this new class of devices is the large margin of improvement that can be envisaged. In particular, for the developed prototype there are a number of issues that can be subject to engineering optimization and improvement. First, the recorded variation of capacitance of the device shows relevant discrepancies with the expected theoretical value. This is attributed to the imperfect evacuation of fluid between the electrodes. Second, losses in the converted energy are recorded which are increasing with electric field and proportional to the duration of the generating phase. One of the greater source of these losses in high voltage tests was found to be charge leakage. Third, limitations in the efficiency are also attributable to viscous losses in the fluid due to sub-optimal fluid dynamic design of the system.

Future devices should consider a redesigned shape of electrodes and fluid channels in order to improve fluid-dynamics aspects. Additionally, improvements of system performance can be achieved by the adoption of enhanced materials. In particular, dielectric fluids with improved permittivity and resistivity, as well as larger dielectric strength should be sought.

In order to achieve such improvements, theoretical studies should be conducted which aim at the development of appropriate coupled multi-physic models that consider both dielectric fluid-dynamics and elastomer electro-elasticity.

Other interesting future studies could also consider solutions for scaling-up the power capabilities of the device. A feasible implementation could be the design of a DFG with multiple units arranged in a stacked layout, creating compact-size devices with adjacent fluid filled chambers featuring alternate pressures.

In conclusion, the promising theoretical predictions, wide margins of performance improvement, and low costs of employed materials, make this novel concept an interesting alternative electromechanical transducer, especially for energy harvesting applications. In the future, the fluido-electric transduction principle described here will also be investigated for actuation and sensing applications.

Acknowledgments

This research received funds from European Commission under the projects WETFEET (H2020 Program, Proj. No. 641334), PolyWEC (Fp7, Program, Proj. No. 309139), and from Tuscany Region (Italy) under the project EOLO (FAR FAS 2014-A). The authors would like to thank Dr Giacomo Moretti and Eng. Francesco Damiani for their technical support.

ORCID iDs

Mattia Duranti https://orcid.org/0000-0003-2345-6177
Michele Righi https://orcid.org/0000-0002-3940-2352
Rocco Vertechy https://orcid.org/0000-0002-0634-1661
Marco Fontana https://orcid.org/0000-0002-5691-8115

References

[1] Jones W 1931 *J. Soc. Motion Pict. Eng.* **16** 3–22
[2] Pister K S, Fearing R S and Howe R T 1990 *Micro Electro Mechanical Systems, 1990. Proc., An Investigation of Micro Structures, Sensors, Actuators, Machines and Robots IEEE* (Piscataway, NJ: IEEE) pp 67–71
[3] Mehregany M, Bart S, Tavrow L, Lang J, Senturia S and Schlecht M 1990 *Sensors Actuators* A **21** 173–9
[4] Philp S F 1977 *IEEE Trans. Electr. Insul.* **EI-12** 130–6
[5] O'Donnell R, Schofield N, Smith A C and Cullen J 2009 *IEEE Trans. Ind. Appl.* **45** 1778–84
[6] Beeby S P, Tudor M J and White N M 2006 *Meas. Sci. Technol.* **17** R175
[7] Kornbluh R D, Pelrine R, Pei Q, Heydt R, Stanford S, Oh S and Eckerle J 2002 *Proc. SPIE* **4698** 254
[8] O'Halloran A, O'Malley F and McHugh P 2008 *J. Appl. Phys.* **104** 9
[9] Koh S J A, Keplinger C, Li T, Bauer S and Suo Z 2011 *IEEE/ASME Trans. Mechatronics* **16** 33–41
[10] Shian S, Huang J, Zhu S and Clarke D R 2014 *Adv. Mater.* **26** 6617–21
[11] Kaltseis R *et al* 2014 *RSC Adv.* **4** 27905–13
[12] Vertechy R, Rosati G P P and Fontana M 2015 *J. Vib. Acoust.* **137** 011004
[13] Peter D, Pichler R, Bauer S and Schwödiauer R 2015 *Extreme Mech. Lett.* **4** 38–44
[14] Larmor J 1892 *Proc. R. Soc.* **52** 55–67
[15] Maxwell J C 1881 *A Teatise on Electricity and Magnetism* vol 1 (Oxford: Clarendon)
[16] Stratton J 1941 *Electromagnetic Theory* (New York: McGraw-Hill)
[17] Landau L D and Lifshitz E 1960 *Course of Theoretical Physics Vol. 8: Electrodynamics of Continuous Media* (Oxford: Pergamon)
[18] Pohl H A and Pohl H 1978 *Dielectrophoresis: The Behavior of Neutral Matter in Nonuniform Electric Fields* vol 80 (Cambridge: Cambridge University Press)
[19] Fan S K, Chen W J, Lin T H, Wang T T and Lin Y C 2009 *Lab Chip* **9** 1590–5
[20] Rosset S, Araromi O A, Schlatter S and Shea H R 2016 *J. Vis. Exp.* **108** e53423
[21] Rosset S and Shea H R 2013 *Appl. Phys.* A **110** 281–307
[22] Perrier C and Beroual A 2009 *IEEE Electr. Insul. Mag.* **25** 6–13
[23] Lide D R (Ed) 2005 Dielectric strength of insulating materials *CRC Handbook of Chemistry and Physics* 85th edn (Boca Raton, FL: CRC)
[24] Bartnikas R 1994 *Electrical Insulating Liquids* (Philadelphia: ASTM)
[25] Dorfmann L and Ogden R W 2014 *Nonlinear Theory of Electroelastic and Magnetoelastic Interactions* (Berlin: Springer) pp 47–90
[26] Grinchik N, Khomich M, Korogoda O, Ivanova S, Terechov V and Grinchik Y N 2011 *Fundamental Problems of the Electrodynamics of Heterogeneous Media with Boundary Conditions Corresponding to the Total-Current Continuity* (Rijeka: Intech)
[27] Pokryvailo A and Carp C 2012 *IEEE Electr. Insul. Mag.* **28** 40–9

[28] La T G, Lau G K, Shiau L L and Tan A W Y 2014 *Smart Mater. Struct.* **23** 105006
[29] Vertechy R, Fontana M, Stiubianu G and Cazacu M 2014 *Proc. SPIE* **9056** 90561R
[30] Pharr M, Sun J Y and Suo Z 2012 *J. Appl. Phys.* **111** 104114
[31] Hossain M, Vu D K and Steinmann P 2015 *Arch. Appl. Mech.* **85** 523–37
[32] Righi M, Vertechy R and Fontana M 2014 *ASME 2014 Conf. on Smart Materials, Adaptive Structures and Intelligent Systems* (American Society of Mechanical Engineers) p V001T03A013
[33] Moretti G, Fontana M and Vertechy R 2015 *J. Intell. Mater. Syst. Struct.* **26** 740–51
[34] Zanini P, Rossiter J and Homer M 2015 *Appl. Phys. Lett.* **107** 153906